Multimode supercontinuum generation in chalcogenide glass fibres

Kubat, Irnis; Bang, Ole

Published in:
Optics Express

Link to article, DOI:
10.1364/OE.24.002513

Publication date:
2016

Document Version
Publisher's PDF, also known as Version of record

Multimode supercontinuum generation in chalcogenide glass fibres

Irnis Kubat* **and Ole Bang**

DTU Fotonik, Danmarks Tekniske Universitet, Ørsteds Plads 343, DK-2800 Kongens Lyngby, Denmark

*ikub@fotonik.dtu.dk

Abstract: Mid-infrared supercontinuum generation is considered in chalcogenide fibres when taking into account both polarisations and the necessary higher order modes. In particular we focus on high pulse energy supercontinuum generation with long pump pulses. The modeling indicates that when only a single polarisation in the fundamental mode is considered the obtainable supercontinuum bandwidth is substantially exaggerated compared to when both polarisations are taken into account. Our modeling shows that if the pump pulse is short enough ($\leq$ 10ps) then higher order modes are not important because of temporal walk-off. In contrast long pump pulses ($\geq$ 40ps) will efficiently excite higher order modes through Raman scattering, which will deplete the fundamental mode of energy and limit the possibility of obtaining a broadband supercontinuum.

OCIS codes: (060.2390) Fiber optics, infrared; (060.4370) Nonlinear optics, fibers; (160.2750) Glass and other amorphous materials

References and links

1. A. B. Seddon, "Mid-infrared (ir) a hot topic: The potential for using mid-ir light for non-invasive early detection of skin cancer in vivo," Phys. Status Solidi B **250**, 1020–1027 (2013).
2. G. Tao, H. Ebendorff-Heidepriem, A. M. Stolyarov, S. Danto, J. V. Badding, Y. Fink, J. Ballato, and A. F. Abouraddy, "Infrared fibers," Adv. Opt. Photon. **7**, 379–458 (2015).
3. J. Faist, F. Capasso, D. L. Sivco, C. Sirtori, A. L. Hutchinson, and A. Y. Cho, "Quantum cascade laser," Science **264**, 553–556 (1994).
4. G. W. Santoni, B. C. Daube, E. A. Kort, R. Jiménez, S. Park, J. V. Pittman, E. Gottlieb, B. Xiang, M. S. Zahniser, D. D. Nelson, J. B. McManus, J. Peischl, T. B. Ryerson, J. S. Holloway, A. E. Andrews, C. Sweeney, B. Hall, E. J. Hintsa, F. L. Moore, J. W. Elkins, D. F. Hurst, B. B. Stephens, J. Bent, and S. C. Wofsy, "Evaluation of the airborne quantum cascade laser spectrometer (qcls) measurements of the carbon and greenhouse gas-suite; co_2, ch_4, n_2o, and co - during the calnex and hippo campaigns," Atmos. Meas. Tech. **7**, 1509–1526 (2014).
5. C. Xia, M. Kumar, M.-Y. Cheng, R. S. Hegde, M. N. Islam, A. Galvanauskas, H. G. Winful, J. Fred L. Terry, M. J. Freeman, M. Poulain, and G. Mazé, "Power scalable mid-infrared supercontinuum generation in zblan fluoride fibers with up to 1.3 watts time-averaged power," Opt. Express **15**, 865–871 (2007).
6. C. Xia, Z. Xu, M. Islam, F. L. Terry, M. Freeman, A. Zakel, and J. Mauricio, "10.5 w time-averaged power mid-ir supercontinuum generation extending beyond 4 μ m with direct pulse pattern modulation," IEEE J. Sel. Top. Quantum Electron. **15**, 422–434 (2009).
7. G. Qin, X. Yan, C. Kito, M. Liao, C. Chaudhari, T. Suzuki, and Y. Ohishi, "Supercontinuum generation spanning over three octaves from uv to 3.85 μm in a fluoride fiber," Opt. Lett. **34**, 2015–2017 (2009).
8. P. M. Moselund, C. Petersen, S. Dupont, C. Agger, O. Bang, and S. R. Keiding, "Supercontinuum: broad as a lamp, bright as a laser, now in the mid-infrared," Proc. SPIE **8381**, 83811A (2012).
9. I. Kubat, C. S. Agger, P. M. Moselund, and O. Bang, "Mid-infrared supercontinuum generation to 4.5 μm in uniform and tapered zblan step-index fibers by direct pumping at 1064 or 1550 nm," J. Opt. Soc. Am. B **30**, 2743–2757 (2013).

#254943 Received 1 Dec 2015; revised 14 Jan 2016; accepted 16 Jan 2016; published 1 Feb 2016

10. R. Thapa, D. Rhonehouse, D. Nguyen, K. Wiersma, C. Smith, J. Zong, and A. Chavez-Pirson, "Mid-ir supercontinuum generation in ultra-low loss, dispersion-zero shifted tellurite glass fiber with extended coverage beyond 4.5 m," Proc. SPIE **8898**, 889808 (2013).
11. X. Jiang, N. Y. Joly, M. A. Finger, F. Babic, G. K. L. Wong, J. C. Travers, and P. S. J. Russell, "Deep-ultraviolet to mid-infrared supercontinuum generated in solid-core zblan photonic crystal fibre," Nature Photon. **9**, 133–139 (2015).
12. J. Hu, C. R. Menyuk, L. B. Shaw, J. S. Sanghera, and I. D. Aggarwal, "Maximizing the bandwidth of supercontinuum generation in as2se3 chalcogenide fibers," Opt. Express **18**, 6722–6739 (2010).
13. R. R. Gattass, L. B. Shaw, V. Nguyen, P. Pureza, I. D. Aggarwal, and J. S. Sanghera, "All-fiber chalcogenide-based mid-infrared supercontinuum source," Optical Fiber Technology **18**, 345–348 (2012).
14. C. Wei, X. Zhu, R. A. Norwood, F. Song, and N. Peyghambarian, "Numerical investigation on high power mid-infrared supercontinuum fiber lasers pumped at 3 μm," Opt. Express **21**, 29488–29504 (2013).
15. M. Bache, H. Guo, and B. Zhou, "Generating mid-ir octave-spanning supercontinua and few-cycle pulses with solitons in phase-mismatched quadratic nonlinear crystals," Opt. Mater. Express **3**, 1647–1657 (2013).
16. I. Kubat, C. R. Petersen, U. V. Møller, A. Seddon, T. Benson, L. Brilland, D. Méchin, P. M. Moselund, and O. Bang, "Thulium pumped mid-infrared 0.9–9μm supercontinuum generation in concatenated fluoride and chalcogenide glass fibers," Opt. Express **22**, 3959–3967 (2014).
17. I. Kubat, C. S. Agger, U. Møller, A. B. Seddon, Z. Tang, S. Sujecki, T. M. Benson, D. Furniss, S. Lamrini, K. Scholle, P. Fuhrberg, B. Napier, M. Farries, J. Ward, P. M. Moselund, and O. Bang, "Mid-infrared supercontinuum generation to 12.5μm in large na chalcogenide step-index fibres pumped at 4.5μm," Opt. Express **22**, 19169–19182 (2014).
18. C. R. Petersen, U. Møller, I. Kubat, B. Zhou, S. Dupont, J. Ramsay, T. Benson, S. Sujecki, N. Abdel-Moneim, Z. Tang, D. Furniss, A. Seddon, and O. Bang, "Mid-infrared supercontinuum covering the 1.4-13.3μm molecular fingerprint region using ultra-high na chalcogenide step-index fibre," Nature Photon. **8**, 830834 (2014).
19. U. Møller, Y. Yu, I. Kubat, C. R. Petersen, X. Gai, L. Brilland, D. Méchin, C. Caillaud, J. Troles, B. Luther-Davies, and O. Bang, "Multi-milliwatt mid-infrared supercontinuum generation in a suspended core chalcogenide fiber," Opt. Express **23**, 3282–3291 (2015).
20. Y. Yu, B. Zhang, X. Gai, C. Zhai, S. Qi, W. Guo, Z. Yang, R. Wang, D.-Y. Choi, S. Madden, and B. Luther-Davies, "1.8-10μm mid-infrared supercontinuum generated in a step-index chalcogenide fiber using low peak pump power," Opt. Lett. **40**, 1081–1084 (2015).
21. J. Price, T. Monro, H. Ebendorff-Heidepriem, F. Poletti, P. Horak, V. Finazzi, J. Leong, P. Petropoulos, J. Flanagan, G. Brambilla, X. Feng, and D. Richardson, "Mid-ir supercontinuum generation from nonsilica microstructured optical fibers," **13**, 738–749 (2007).
22. B. Temelkuran, S. D. Hart, G. Benoit, J. D. Joannopoulos, and Y. Fink, Nature **420**, 650–653 (2002).
23. C. Markos, S. N. Yannopoulos, and K. Vlachos, "Chalcogenide glass layers in silica photonic crystal fibers," Opt. Express **20**, 14814–14824 (2012).
24. C. Markos, I. Kubat, and O. Bang, "Hybrid polymer photonic crystal fiber with integrated chalcogenide glass nanofilms," Sci. Rep. **4**, 6057 (2014).
25. H. G. Dantanarayana, N. Abdel-Moneim, Z. Tang, L. Sojka, S. Sujecki, D. Furniss, A. B. Seddon, I. Kubat, O. Bang, and T. M. Benson, "Refractive index dispersion of chalcogenide glasses for ultra-high numerical-aperture fiber for mid-infrared supercontinuum generation," Opt. Mater. Express **4**, 1444–1455 (2014).
26. T. Hu, D. D. Hudson, and S. D. Jackson, "Actively q-switched 2.9 μm ho 3+ pr 3+-doped fluoride fiber laser," Opt. Lett **37**, 2145–2147 (2012).
27. T. Hu, D. D. Hudson, and S. D. Jackson, "Stable, self-starting, passively mode-locked fiber ring laser of the 3 μm class," Opt. Lett. **39**, 2133–2136 (2014).
28. Y. Yu, X. Gai, P. Ma, D.-Y. Choi, Z. Yang, R. Wang, S. Debbarma, S. J. Madden, and B. Luther-Davies, "A broadband, quasi-continuous, mid-infrared supercontinuum generated in a chalcogenide glass waveguide," Laser Photon. Rev. **8**, 792–798 (2014).
29. S. D. Jackson, "Towards high-power mid-infrared emission from a fibre laser," Nature Photon. **6**, 423–431 (2012).
30. T. Wang, X. Gai, W. Wei, R. Wang, Z. Yang, X. Shen, S. Madden, and B. Luther-Davies, "Systematic z-scan measurements of the third order nonlinearity of chalcogenide glasses," Opt. Mater. Express **4**, 1011–1022 (2014).
31. J. Troles, Q. Coulombier, G. Canat, M. Duhant, W. Renard, P. Toupin, L. Calvez, G. Renversez, F. Smektala, M. E. Amraoui, J. L. Adam, T. Chartier, D. Mechin, and L. Brilland, "Low loss microstructured chalcogenide fibers for large non linear effects at 1995 nm," Opt. Express **18**, 26647–26654 (2010).
32. B. Zhang, W. Guo, Y. Yu, C. Zhai, S. Qi, A. Yang, L. Li, Z. Yang, R. Wang, D. Tang, G. Tao, and B. Luther-Davies, "Low loss, high na chalcogenide glass fibers for broadband mid-infrared supercontinuum generation," J. Am. Ceram. Soc. **98**, 1389–1392 (2015).
33. Z. Tang, V. S. Shiryaev, D. Furniss, L. Sojka, S. Sujecki, T. M. Benson, A. B. Seddon, and M. F. Churbanov, "Low loss ge-as-se chalcogenide glass fiber, fabricated using extruded preform, for mid-infrared photonics," Opt. Mater. Express **5**, 1722–1737 (2015).
34. S. Coen, A. H. L. Chau, R. Leonhardt, J. D. Harvey, J. C. Knight, W. J. Wadsworth, and P. S. J. Russell, "Supercontinuum generation by stimulated raman scattering and parametric four-wave mixing in photonic crystal

#254943 Received 1 Dec 2015; revised 14 Jan 2016; accepted 16 Jan 2016; published 1 Feb 2016

fibers," J. Opt. Soc. Am. B **19**, 753–764 (2002).
35. M. Grabka, B. Wajnchold, S. Pustelny, and W. Gawlik, "Experimental and theoretical study of light propagation in suspended-core optical fiber," Acta. Phys. Pol. A **118**, 1647–1657 (2010).
36. J. Ramsay, S. Dupont, M. Johansen, L. Rishøj, K. Rottwitt, P. M. Moselund, and S. R. Keiding, "Generation of infrared supercontinuum radiation: spatial mode dispersion and higher-order mode propagation in zblan step-index fibers," Opt. Express **21**, 10764–10771 (2013).
37. I. Shavrin, S. Novotny, and H. Ludvigsen, "Mode excitation and supercontinuum generation in a few-mode suspended-core fiber," Opt. Express **21**, 32141–32150 (2013).
38. K. S. Chiang, "Stimulated raman scattering in a multimode optical fiber: evolution of modes in stokes waves," Opt. Lett. **17**, 352–354 (1992).
39. A. Sharma, M. Dokhanian, Z. Wu, R. Posey, A. Williams, and P. Venkateswarlu, "Stimulated raman scattering in a multimode optical fiber with bend-induced loss," Opt. Commun. **111**, 127–131 (1994).
40. H. Pourbeyram, G. P. Agrawal, and A. Mafi, "Stimulated raman scattering cascade spanning the wavelength range of 523 to 1750nm using a graded-index multimode optical fiber," Appl. Phys. Lett. **102**, 201107 (2013).
41. F. Poletti and P. Horak, "Dynamics of femtosecond supercontinuum generation in multimode fibers," Opt. Express **17**, 6134–6147 (2009).
42. P.-A. Champert, V. Couderc, P. Leproux, S. Février, V. Tombelaine, L. Labonté, P. Roy, C. Froehly, and P. Nérin, "White-light supercontinuum generation in normally dispersive optical fiber using original multi-wavelength pumping system," Opt. Express **12**, 4366–4371 (2004).
43. R. T. White and T. M. Monro, "Cascaded raman shifting of high-peak-power nanosecond pulses in as2s3 and as2se3 optical fibers," Opt. Lett. **36**, 2351–2353 (2011).
44. F. Poletti and P. Horak, "Description of ultrashort pulse propagation in multimode optical fibers," J. Opt. Soc. Am. B **25**, 1645–1654 (2008).
45. R. Khakimov, I. Shavrin, S. Novotny, M. Kaivola, and H. Ludvigsen, "Numerical solver for supercontinuum generation in multimode optical fibers," Opt. Express **21**, 14388–14398 (2013).
46. Irflex inc.,"arsenic selenide fibre loss," http://www.irflex.com/.
47. B. Ung and M. Skorobogatiy, "Chalcogenide microporous fibers for linear and nonlinear applications in the mid-infrared," Opt. Express **18**, 8647–8659 (2010).
48. E. A. Romanova, Y. S. Kuzyutkina, A. I. Konyukhov, N. Abdel-Moneim, A. B. Seddon, T. M. Benson, S. Guizard, and A. Mouskeftaras, "Nonlinear optical response and heating of chalcogenide glasses upon irradiation by the ultrashort laser pulses," Opt. Eng. **53**, 071812 (2014).
49. M. H. Frosz, P. Falk, and O. Bang, "The role of the second zero-dispersion wavelength in generation of supercontinua and bright-bright soliton-pairs across the zero-dispersion wavelength," Opt. Express **13**, 6181–6192 (2005).
50. G. P. Agrawal, "Nonlinear Fiber Optics," 4th ed. (Elsevier, 2007).
51. E. A. Golovchenko and A. N. Pilipetskii, "Unified analysis of four-photon mixing, modulational instability, and stimulated raman scattering under various polarization conditions in fibers," J. Opt. Soc. Am. B **11**, 92–101 (1994).
52. R. Hellwarth, "Third-order optical susceptibilities of liquids and solids," Prog. Quantum Electron. **5**, 1–68 (1977).

1. Introduction

The mid-infrared (mid-IR) frequency range from 2 to 15μm is of great importance for applications, such as early stage cancer detection, spectroscopy on organic and in-organics molecules, air-pollution monitoring, and infrared counter measures [1,2]. Previously, this was much an unreachable wavelength range due to the lack of high power and spatially coherent laser sources. With the advent of the quantum cascade lasers (QCL) [3] this wavelength region began to be probed. This allowed for some quite fascinating research to be conducted such as mounting the QCLs on airplanes and monitoring green house gasses during flight [4]. While the QCLs opened a new frontier in mid-IR spectroscopy the QCLs operate at a narrow spectral range around the emission wavelength. In the past decade a lot of ground has been covered theoretically and experimentally in devising mid-IR broadband supercontinuum laser sources based on mid-IR glasses out to 5 and 10μm and beyond in fluoride/tellurites [5–11] and chalcogenides [12–20], respectively, as these are transparent in different regions of the mid-IR spectrum. Especially, the chalcogenide glasses are considered ideal for mid-IR nonlinear frequency conversion due to their much wider mid-IR transparency window and stronger nonlinearities when compared to standard silica fibres [21]. Chalcogenides may also be deposited in liquid phase into the holes

#254943 Received 1 Dec 2015; revised 14 Jan 2016; accepted 16 Jan 2016; published 1 Feb 2016

of silica or polymer PCF to make multi-functional multi-material fibres [22–24].

The most efficient supercontinuum generation is obtained with a pump laser wavelength close to the first zero dispersion wavelength (ZDW) of the fibre. For chalcogenide fibres this is challenging as most commercial lasers operate in the near-IR, such as the ytterbium laser at 1μm, the erbium laser at 1.55μm and the thulium laser at 2μm, which are too far away from the material ZDW of the chalcogenides (e.g., 7μm for As-Se [25]). New types of 3μm [26,27] and 4μm [28] pulsed lasers are now being developed, which are coming closer to the material ZDW of the chalcogenides [29]. However, engineering on the fibre side is still necessary to bridge the gap between the laser lines and the chalcogenide fibres ZDW. Chalcogenides fibres can be made of several glass compositions with different linear and nonlinear properties [30], which allows to move the ZDW significantly by increasing the index contrast between the core and cladding materials [25]. The ZDW of chalcogenide fibres can also be tuned using microstructured fibre designs [31].

In order to obtain mid-IR supercontinuum generation high NA fibres are needed to lower the ZDW and keep the light confined at long wavelength, which makes the fibres multimoded. The state-of-the art high NA chalcogenide step-index fibres have an NA as high as 1.3 [25, 32, 33] and are not polarisation maintaining. Ideally, the supercontinuum should be generated only in one polarisation to yield the broadest spectrum possible [34]. Furthermore, in multimode fibres power can be lost to higher order mode (HOM) during in-coupling [35–37], or coupling between fibre modes due to nonlinear effects along the fibre. The nonlinear coupling can either be through intermodal Raman scattering [38–40] or through four wave mixing (FMW) between modes [18, 41].

In this work we numerically consider high pulse energy mid-IR supercontinuum with long pump pulses in a multimode high NA chalcogenide fibre. The fibre has an NA of 1.0 and ZDW of 5μm [17], and we pump at 2.9μm, which represent the pump wavelength of several emerging mid-IR lasers, such as Er^{3+}, Ho^{3+}, Pr^{3+} and Dy^{3+} doped ZBLAN lasers [29]. This means that we are pumping in the normal dispersion regime and must rely on mainly Raman scattering to transfer power across the ZDW and achieve supercontinuum generation. A Raman cascade with seven Raman lines has been demonstrated in silica fibres [42] while four Raman lines have been demonstrated in chalcogenide fibres [43]. If the Raman cascade can transfer enough power across the ZDW this could potentially be a promising design for mid-IR supercontinuum sources.

Advanced modeling is typically used to design supercontinuum sources. However, in the mid-IR this has so far only been based on the scalar model. In this work we take into account HOMs and both polarisations, and we determine, which HOMs that must be considered. We consider 10-60ps pump pulses to determine the effect of temporal walk-off on the excitation of HOMs and the resulting supercontinuum bandwidth. We demonstrate that for pulses shorter than 10ps excitation of HOMs is negligible, while for pulses longer than 40ps HOMs are efficiently excited and severely deplete the power in the fundamental mode.

2. Modeling multimode nonlinear effects

The modeling was done by solving the multimode generalised nonlinear Schrödinger equation (MM-GNLSE) [41, 44, 45]

$$\begin{aligned}\frac{\partial \tilde{A}_p(z,\Omega)}{\partial z} &= i[\tilde{\beta}^{(p)}(\omega)-\alpha^{(p)}(\omega)/2]\tilde{A}_p(z,\Omega)+\\ i\frac{n_2\omega_0}{c}(1+\frac{\Omega}{\omega_0})\sum_{lmn}F\Big\{2Q^{(1)}_{plmn}(\omega_0)A_l(T)R*(A_mA_n^*)+(1-f_R)Q^{(2)}_{plmn}(\omega_0)A_l^*(T)A_m(T)A_n(T)\Big\} &\qquad (1)\\ &= i[\hat{D}+\hat{N}]\tilde{A}(z,\Omega),\end{aligned}$$

#254943 Received 1 Dec 2015; revised 14 Jan 2016; accepted 16 Jan 2016; published 1 Feb 2016

$\tilde{\beta}^{(p)}(\omega) = \beta^{(p)}(\omega) - \beta^{(1)}(\omega_0) - \beta_1^{(1)}(\omega_p)\Omega$ with $\alpha^{(p)}(\omega) = \alpha_m(\omega) + \alpha_{cf}^{(p)}(\omega)$ where $\alpha_m(\omega)$ was a constant background loss chosen here to be 1dB/m. Such a low loss is now becoming readily available [32, 33, 46]. The loss $\alpha_{cf}^{(p)}(\omega)$ was the confinement loss for the individual modes. The coupled equations were written in a reference frame moving with the velocity of the fundamental LP_{01} mode (p=1). The dispersive operator $\hat{D}$ takes into account the dispersion, the loss and the group velocity mismatch between the modes. The nonlinear operator $\hat{N}$ took into account the nonlinear coupling between modes due to cross phase modulation (XPM), FWM as well as Raman scattering given as $R(T) = (1 - f_R)\delta(T) + 3/2h(T)$. $F[...]$ denotes Fourier transform. The overlap integrals $Q_{plmn}^{(1)}$ and $Q_{plmn}^{(2)}$ are given as

$$
\begin{aligned}
Q_{plmn}^{(1)}(\omega) &= \frac{\varepsilon_0^2 n_0^2 c^2}{12} \frac{\int\int [\tilde{\mathbf{F}}_p^*(x,y,\omega)\cdot\tilde{\mathbf{F}}_l(x,y,\omega)][\tilde{\mathbf{F}}_m(x,y,\omega)\cdot\tilde{\mathbf{F}}_n^*(x,y,\omega)]dxdy}{N_p(\omega)N_l(\omega)N_m(\omega)N_n(\omega)} \\
Q_{plmn}^{(2)}(\omega) &= \frac{\varepsilon_0^2 n_0^2 c^2}{12} \frac{\int\int [\tilde{\mathbf{F}}_p^*(x,y,\omega)\cdot\tilde{\mathbf{F}}_l^*(x,y,\omega)][\tilde{\mathbf{F}}_m(x,y,\omega)\cdot\tilde{\mathbf{F}}_n(x,y,\omega)]dxdy}{N_p(\omega)N_l(\omega)N_m(\omega)N_n(\omega)} \\
N_i^2(\omega) &= \frac{1}{4}\int \left[\tilde{\mathbf{F}}_i^*(x,y,\omega)\times\tilde{\mathbf{H}}_i(x,y,\omega) + \tilde{\mathbf{F}}_i(x,y,\omega)\times\tilde{\mathbf{H}}_i^*(x,y,\omega)\right]\cdot\mathbf{e}_z dxdy, \\
& \quad i = (p,l,m,n),
\end{aligned}
\tag{2}
$$

where $\tilde{\mathbf{F}}_p(x,y,\omega)$ are the transverse components of the total electric field $\tilde{\mathbf{E}}_p(x,y,z,\omega) = \tilde{\mathbf{F}}_p(x,y,\omega)\tilde{A}_p(z,\omega)e^{i\lambda^{(p)}z}$ and $\tilde{\mathbf{H}}_p(x,y,\omega)$ are the corresponding mode transverse component of the total magnetic field. Both $\tilde{\mathbf{F}}_p(x,y,\omega)$, $\tilde{\mathbf{H}}_p(x,y,\omega)$, and $\lambda^{(p)}(\omega) = -i\beta^{(p)}(\omega) - \alpha_{cf}^{(p)}(\omega)$ were obtained using the commercial finite element method (FEM) tool COMSOL®.

In this work state-of-the art chalcogenide step-index fibres with NA of 1.0 were considered. Such high NA fibres based on As-Se and Ge-As-Se have only recently become experimentally feasible as the core and the cladding materials needed have be sufficiently different refractive indices while at the same time being thermally compatible so that they could be drawn together into a fibre [25]. The refractive indices of the core As-Se glass and the cladding Ge-As-Se glass are taken from [25]. The Raman response function for the As-Se glass was taken from [47]. The Kerr coefficient for the same glass was taken from [48].

A thorough design optimisation of step-index fibres based on these chalcogenide glasses showed how increasing the core-cladding index difference allowed for engineering the dispersion and move the first ZDW to shorter wavelengths [17]. In particular the calculations showed that the first ZDW went down to around 5μm in a fibre with a core diameter of 8μm and NA of 1.0. Initial scalar supercontinuum modeling showed that this fibre could generate a supercontinuum out to 12.5μm when pumped with 50ps pulses at 4.5μm in the normal dispersion regime. Here we use use full dual polarisation multimode modeling of supercontinuum generation pumped at 2.9μm with 10-60ps pulses. The aim is to investigate the realistic supercontinuum performance of this fibre when pumped at 2.9μm, and the general influence of the second polarisation and the higher order modes on supercontinuum generation pumped with long pulses in the normal dispersion regime.

The dispersion and modal profiles of guided modes of the 8μm core diameter high NA As-Se fibre are shown in Fig. 1(a). The FEM modeling of the dispersion for the LP_{01} mode in a similar fibre was previously confirmed experimentally [18]. Not all the guided modes are shown here as they were either two-fold degenerate, such as for the concentric LP_{0n} modes, or four-fold degenerate such as the other modes. The dispersion profiles show that the 2.9μm pump is deep in the normal dispersion regime of the LP_{01} mode while it is within two Raman order of the anomalous dispersion of the LP_{21} and LP_{02} modes. For the even higher order modes the dispersion is all-normal. Since the supercontinuum generation is most efficient in

#254943 Received 1 Dec 2015; revised 14 Jan 2016; accepted 16 Jan 2016; published 1 Feb 2016

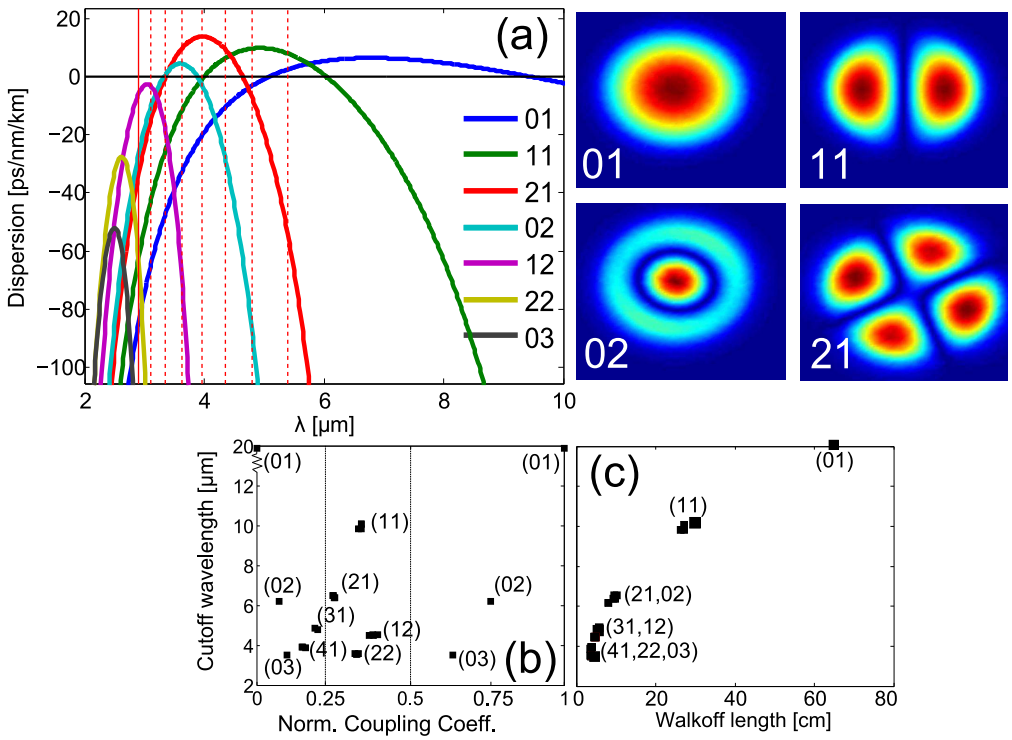

Fig. 1. (a) Dispersion of the guided modes in a 8μm core diameter fibre with NA=1.0 with the power distribution of the transverse field component to the right. The vertical solid line is the 2.9μm pump and the dashed lines are the first seven Raman stokes orders. (b) Normalised coupling coefficient versus cutoff wavelength for the different modes. The dashed vertical lines mark the 25 and 50% coupling limits. (c) Walk-off length between the pump at 2.9μm in the LP_{01} mode and the first Raman line at 3.1μm in the higher order modes versus their respective cutoff wavelengths for a 10ps pump pulse.

the anomalous dispersion regime the dispersion profiles alone indicate that we should consider the influence of the $LP_{01,11,21,02}$ modes.

Because we pump in the normal dispersion regime with long pulses temporal walk-off is weak and Raman scattering becomes important. In particular, Raman scattering is known to be able to couple different spatial modes together [40]. The Raman scattering is dependent on the spatial distribution of the modes involved in the scattering process. In order to further look into which of the modes are relevant to consider in the supercontinuum modeling the normalised coupling coefficient from the LP_{01} mode containing the pump pulse (number 1) to the mode number m given as $\bar{Q}_m^{(1)} = Q_{1m1m}^{(1)}/Q_{1111}^{(1)}$.

was therefore computed and shown in Fig. 1(b). Here the number in the parenthesis indicates the mode number m. Two m=(01,02,03) coefficients appear due to the two polarisations and four appear for the other modes due to degeneracy and two polarisations.

Figure 1(b) shows the normalised coupling coefficient and the cutoff wavelength of the individual modes. The modes that coupled the strongest were the three concentric LP_{0n} modes co-polarised with the LP_{01} polarisation containing the pump pulse. This was followed by the four-fold degenerate $LP_{11,21,12,22}$ modes, which had a normalised coupling coefficient from 25 to 50%. All other modes had a normalised coupling coefficient below 25%. The normalised

#254943 Received 1 Dec 2015; revised 14 Jan 2016; accepted 16 Jan 2016; published 1 Feb 2016

coupling coefficients indicate that we need to consider seven modes. However, even though the mode is excited its importance might be restricted if it is not guided to sufficiently long wavelengths. This indicates that only the $LP_{01,11,21,02}$ modes need to be considered as they have a cutoff above 6μm where as the rest have a cutoff below 5μm.

To make a final decision we look at the walk-off length between the pump at 2.9μm and the first Raman line at 3.1μm in the higher order modes, given by $L_W = T_0/|\beta_1^1(\omega_p) - \beta_1^m(\omega_R)|$. Here T_0 is the pump pulse duration and $\beta_1^m(\omega_R)$ is the inverse group velocity for mode m at frequency ω_R. The calculated L_W for a 10ps pulse is shown in Fig. 1(c), which confirms that we can restrict our selves to consider only the $LP_{01,11,21,02}$ modes as also predicted by the dispersion profiles.

3. Supercontinuum generation in the LP_{01} mode

Initially, we consider the conventional scalar single-mode modeling of the supercontinuum generation, assuming excitation of only the fundamental LP_{01} mode [35, 38]. In this case the MM-GNLSE was reduced to

$$\frac{\partial \tilde{A}(z,\Omega)}{\partial z} = i[\tilde{\beta}(\omega) - \alpha(\omega)/2]\tilde{A}(z,\Omega) + i\gamma\left(1+\frac{\Omega}{\omega_0}\right)F[A(z,T)\int R(T-T')|A(z,T)|^2 dT'], \qquad (3)$$

where $\tilde{\beta}(\omega) = \beta(\omega) - \beta(\omega_0) - \beta_1(\omega_p)\Omega$.

In Fig. 2 we shown the results of modeling for a pump pulse of 4.8kW peak power having 10, 20, 40 and 60ps pulse duration.

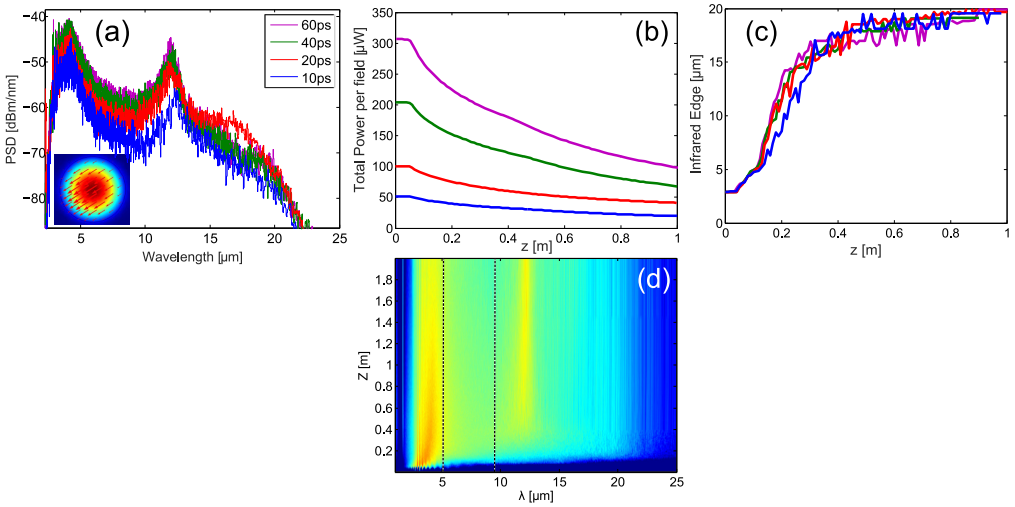

Fig. 2. (a) Supercontinuum spectra after 1m of fibre. Inset: LP_{01} mode and polarisation. (b) Total power as function of propagation length. (c) Infrared edge evaluated at -30dB as function of propagation length. (d) Contour plot of the developing supercontinuum up to 2m for a 60ps pump pulse. The dashed lines represent the ZDWs on the fibre.

For increasingly longer pulse duration the power spectral density is increasing due to the increasing pulse energy. The spectral profile remains the same reflective that the fibre was fixed, and that the spectral broadening mechanism was always the same. Due to the very weak dispersion and strong nonlinearity the nonlinear dynamics in the anomalous dispersion regime will be dominated by SPM, and the solitons that will be generated will quickly red shift to

#254943 Received 1 Dec 2015; revised 14 Jan 2016; accepted 16 Jan 2016; published 1 Feb 2016

the second ZDW and generate dispersive waves in the normal dispersion regime just above the ZDW. Both effects deplete the signal in between the two ZDWs, and generate peaks just outside the anomalous dispersion regime [49] (here at 4 and 12μm).

The evaluated total power shown in Fig. 1(b) was continually decreasing due to loss and the strong broadening to longer wavelengths which likewise decrease the pulse energy. The evaluated long wavelength edge at -30dB is shown in Fig. 1(c) for the different pulse durations. For all the different pulse durations the continuum extended to 20μm and beyond.

The dynamics of the whole continuum generation is shown in Fig. 1(d) where initially a strong Raman cascade is seen to distribute the light across much of the transmission window of the fibre. At least six Raman stokes orders given by the dashed lines appear initially. Such strong cascade has been previously demonstrated by White *et al.* where they generated up to five Raman orders in a sulfide fibre pumped at 2μm [43].

The modeling was then extended to include both polarisations of the fundamental mode. The MM-GNLSE in Eq. (1) is in this case reduced to two coupled GNLSE, one for each polarisation, given as

$$\begin{aligned}
\frac{\partial \tilde{A}_1(z,\Omega)}{\partial z} &= i[\tilde{\beta}^{(1)}(\omega)-\alpha^{(1)}(\omega)/2]\tilde{A}_1(z,\Omega) \\
&\quad + i\gamma\left(1+\frac{\Omega}{\omega_0}\right)F[(1-f_R)A_1(T)(|A_1(T)|^2+\frac{2}{3}|A_2(T)|^2)\times \\
&\quad + f_R A_1(T)h*(|A_1|^2+|A_2|^2)+(1-f_R)\frac{1}{3}A_1^*(T)A_2^2(T)] \\
\frac{\partial \tilde{A}_2(z,\Omega)}{\partial z} &= i[\tilde{\beta}^{(2)}(\omega)-\alpha^{(2)}(\omega)/2]\tilde{A}_2(z,\Omega) \\
&\quad + i\gamma\left(1+\frac{\Omega}{\omega_0}\right)F[(1-f_R)A_2(T)(|A_2(T)|^2+\frac{2}{3}|A_1(T)|^2)\times \\
&\quad f_R A_2(T)h*(|A_2|^2+|A_1|^2)+(1-f_R)\frac{1}{3}A_2^*(T)A_1^2(T)],
\end{aligned} \tag{4}$$

where $\tilde{\beta}^{(j)}(\omega)=\beta^{(j)}(\omega)-\beta^{(1)}(\omega_0)-\beta_1^1(\omega_p)\Omega, \quad j=(1,2)$. The two polarisations $\tilde{A}_1(z,\Omega)$ and $\tilde{A}_2(z,\Omega)$ are coupled with each other through XPM and FWM. This model is the same as the one used previously to study polarisation effects in fibres [34, 50]. The pump pulses used previously in the single polarisation case were coupled into one of the polarisation of the LP_{01} mode and propagated over one meter of fibre.

Figure 3 shows simulated supercontinuum for four different pulse durations. Figure 3(a) shows the supercontinuum spectrum for the total field. As anticipated from the work of Coen *et al*. [34] we observe a significantly reduced spectral broadening because the power is rapidly distributed evenly between the polarisations. Figure 3(b) shows that the power equilibrium is obtained after 1 meter of fibre for all pulse durations, and that the equilibrium length increases with the pulse duration. In contrast Fig. 3(c) shows that the two polarisations obtained the same bandwidth already after 20cm.

More detail on the developing supercontinuum is seen in Figs. 3(d)–3(e), which show the contour plots of the dynamics of the two polarisations. In the polarisation with the pump pulse two Raman lines build up within the first 20cm at 3.11 and 3.35μm (solid black lines in Fig. 3(d)) while at the same time FWM stokes and anti-stokes in the orthogonal polarisation build up (red lines in Fig. 3(e)) around the pump. This was followed by a build up of a Raman line at at 3.22μm where the FWM stokes at 3μm acted as a pump. The presence of FWM stokes and anti-stokes lines in the orthogonal polarisation due to polarisation modulation instability (PMI) when pumping in the normal dispersion regime of the fiber is well-known [51]. The PMI gain

#254943 Received 1 Dec 2015; revised 14 Jan 2016; accepted 16 Jan 2016; published 1 Feb 2016

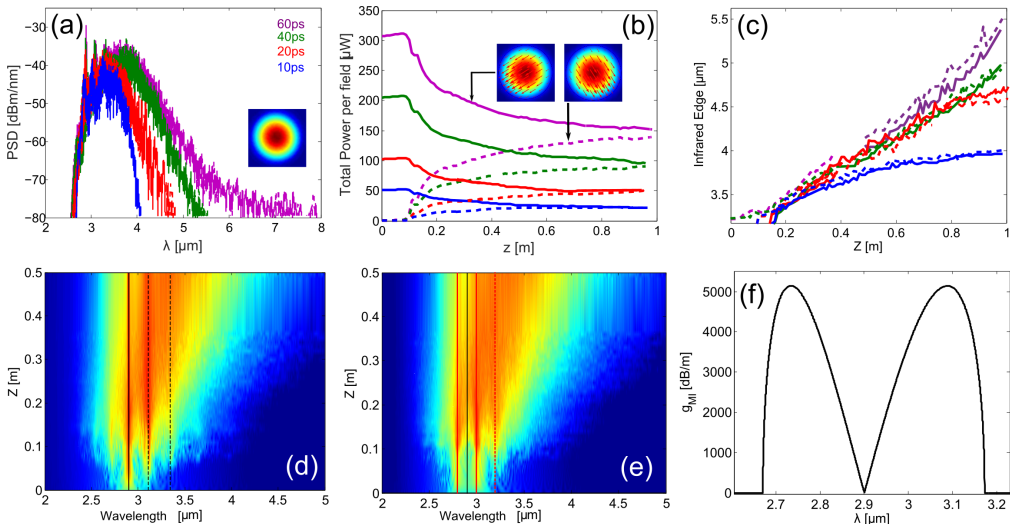

Fig. 3. (a) Supercontinuum spectra after one meter of fibre for different pump pulse durations. Inset: intensity distribution of the LP_{01} mode. (b) Power in the pump (solid) and the orthogonal (dashed) polarisations. Inset: Intensity distribution and polarisation for the two polarisations. (c) Infrared edge evaluated at -30dB for the two polarisations. (d)-(e) Contour plots of the developing continuum for the 60ps pulse for the polarisation with the pump pulse and of the orthogonal polarisation, respectively. Dashed and solid black lines are the pump and Raman stokes, respectively, the red lines are the FWM stokes and anti-stokes occurring in the orthogonal polarisation. (f) PMI gain band corresponding to the sidebands (solid red) in (e).

$g_{PMI} = R(K)$ can be calculated from the formula

$$\left[K - i\Omega/\omega_p\gamma P_0\left(\frac{2}{3}(1-f_R)+f_R\right)\right]^2 = -(\Delta\beta/2)^2 - (1-f_R)\frac{1}{3}\left((\Delta\beta/2)+(\Omega/\omega_p\gamma P_0)^2\right), \qquad (5)$$

with the phase matching term given as $\Delta\beta = 2(n_1 - n_2)\omega_p/c - \beta_2\Omega^2$ where n_1 and n_2 are the refractive indices for the two polarisations of LP_{01}. The PMI gain is shown in Fig. 3(f), and confirms the 2.9 and 3μm side bands observed in Fig. 3(e).

Comparison between the results for the single polarisation in Fig. 2 and having both polarisation in Fig. 3 of LP_{01} illustrated the importance of having both polarisation of the fundamental mode in the simulations as the Raman scattering within one polarisation and the FWM between both polarisation compete against each either, and here the transfer of light between the orthogonal polarisation worked at the same rate as the Raman scattering occurring within the polarisation having the pump pulse thereby limiting the ability for the same broadening to take place as was seen in the single mode and single polarisation case shown in Fig. 2. It should be noted the modeling here was for an ideal fibre having almost no birefringence other than the numerical birefringence occurring in the modeling and therefore with phase matching between the polarisations. In reality a mixture between the two presented scenarios would be expected, since in non-perfect fibres the phase matching between the two polarisations would probably not be so perfect.

#254943 Received 1 Dec 2015; revised 14 Jan 2016; accepted 16 Jan 2016; published 1 Feb 2016

4. Supercontinuum generation in the $LP_{01,11,21,02}$ modes

Supercontinuum generation was then studied in the selected most important $LP_{01,11,21,02}$ modes in order to estimate the influence of the intermodal coupling processes on the formation of supercontinuum. As was discussed previously the pump light coupled into only the LP_{01} mode under optimum launch conditions, will due to a long walk-off length between the modes and strong intermodal coupling transfer light into the HOMs. As the pump durations is long and is located in the normal dispersion regime Raman scattering will be an important mechanism in transferring energy between the modes. This has previously been studied experimentally in silica fibres where different Raman orders occurred in different modes [40]. Raman scattering depends on the pulse duration so here both short and long pulses are investigated in order to quantify the necessary pulse durations needed for either enhancing or inhibiting intermodal energy transfers.

Initially, we considered the $LP_{01,02}$ modal interactions as these had the strongest intermodal Raman coupling coefficients. Expanding Eq. (1) with the strongest overlap integrals when considering two modes each with two polarisations coupled through intermodal Raman scattering yielded

$$
\begin{aligned}
\frac{\partial \tilde{A}_1(z,\Omega)}{\partial z} &= i\left[\tilde{\beta}^{(1)}(\omega)+i\alpha^{(1)}(\omega)/2\right]\tilde{A_1}(z,\Omega)+i\frac{n_2\omega_0}{c}(1+\frac{\Omega}{\omega_0})F(2(Q^{(1)}_{1111}R*(A_1A_1^*)+\cdots\\
&+Q^{(1)}_{1144}R*(A_4A_4^*))A_1+2(Q^{(1)}_{1313}R*(A_1A_3^*)+Q^{(1)}_{1331}R*(A_3A_1^*))A_3+(1-f_R)(Q^{(2)}_{1111}A_1A_1+\cdots\\
&+Q^{(2)}_{1144}A_4A_4)A_1^*+(1-f_R)(Q^{(2)}_{1313}A_1A_3+Q^{(2)}_{1331}A_3A_1)A_3^*)\\
\frac{\partial \tilde{A}_2(z,\Omega)}{\partial z} &= i\left[\tilde{\beta}^{(2)}(\omega)+i\alpha^{(2)}(\omega)/2\right](\omega)\tilde{A_2}(z,\Omega)+i\frac{n_2\omega_0}{c}(1+\frac{\Omega}{\omega_0})F(2(Q^{(1)}_{2211}R*(A_1A_1^*)+\cdots\\
&+Q^{(1)}_{2244}R*(A_4A_4^*))A_2+2(Q^{(1)}_{2424}R*(A_2A_4^*)+Q^{(1)}_{2442}R*(A_4A_2^*))A_4+(1-f_R)(Q^{(2)}_{2222}A_2A_2+\cdots\\
&+Q^{(2)}_{2244}A_4A_4)A_2^*+(1-f_R)(Q^{(2)}_{2424}A_2A_4+Q^{(2)}_{2442}A_4A_2)A_4^*)\\
\frac{\partial \tilde{A}_3(z,\Omega)}{\partial z} &= i\left[\tilde{\beta}^{(3)}(\omega)+i\alpha^{(3)}(\omega)/2\right]\tilde{A_3}(z,\Omega)+i\frac{n_2\omega_0}{c}(1+\frac{\Omega}{\omega_0})F(2(Q^{(1)}_{3311}R*(A_1A_1^*)+\cdots\\
&+Q^{(1)}_{3344}R*(A_4A_4^*))A_3+2(Q^{(1)}_{3131}R*(A_3A_1^*)+Q^{(1)}_{3113}R*(A_1A_3^*))A_1+(1-f_R)(Q^{(2)}_{3333}A_3A_3+\cdots\\
&+Q^{(2)}_{3344}A_4A_4)A_3^*+(1-f_R)(Q^{(2)}_{3131}A_3A_1+Q^{(2)}_{3113}A_1A_3)A_1^*\\
\frac{\partial \tilde{A}_4(z,\Omega)}{\partial z} &= i\left[\tilde{\beta}^{(4)}(\omega)+i\alpha^{(4)}(\omega)/2\right]\tilde{A_4}(z,\Omega)+i\frac{n_2\omega_0}{c}(1+\frac{\Omega}{\omega_0})F(2(Q^{(1)}_{4411}R*(A_1A_1^*)+\cdots\\
&+Q^{(1)}_{4444}R*(A_4A_4^*))A_4+2(Q^{(1)}_{4242}R*(A_4A_2^*)+Q^{(1)}_{4224}R*(A_2A_4^*))A_2+(1-f_R)(Q^{(2)}_{4411}A_1A_1+\cdots\\
&+Q^{(2)}_{4444}A_4A_4)A_4^*+(1-f_R)(Q^{(2)}_{4242}A_4A_2+Q^{(2)}_{4224}A_2A_4)A_2^*).
\end{aligned}
\tag{6}
$$

The fields 1 and 2 are the two polarisation of LP_{01}, and 3 and 4 are the two LP_{02} polarisations. The overlap integrals $Q^{(1)}_{pppp}$ and $Q^{(1)}_{ppqq}$ represent the nonlinear SPM, XPM, and Raman coupling. The $Q^{(2)}$ overlap integrals contribute with additional SPM, XPM and intermodal FWM. The overlap integrals on the form $Q^{(1)}_{pqpq}$ are of interest as these are responsible for the Raman induced power transfer between the modes. These were also the ones being plotted in Fig. 1(b). In Eq. (6) we neglected the weak Raman induced cross-polarisation coupling ($Q^{(1,2)}_{1414}=Q^{(1,2)}_{2323}=Q^{(1,2)}_{4141}=Q^{(1,2)}_{3232}$=0) and assumed that Raman induced coupling only takes place between the same polarisations ($Q^{(1,2)}_{1313}=Q^{(1,2)}_{3131}\neq 0, Q^{(1,2)}_{2424}=Q^{(1,2)}_{4242}\neq 0$).

It should be noted that Eq. (1) does not fully take into account the full tensor nature of the Raman response, but approximates the cross-polarised part with the co-polarised part, so that only the co-polarised Raman function describes all the Raman induced effect [44]. However, the intermodal couplings that are responsible for the power exchange, are actually related to

#254943 Received 1 Dec 2015; revised 14 Jan 2016; accepted 16 Jan 2016; published 1 Feb 2016

the orthogonally polarised Raman response [52]. For conventional fused silica glass the orthogonal Raman gain is lower than the co-polarised Raman at the peak gain frequency. If the same applies for chalcogenides this means that the Raman power transfer in the simulations is overestimated. However, as there is no measurements of the orthogonal Raman gain of the As_2Se_3 chalcogenide currently available in the literature, the co-polarised one was used for all the Raman interactions.

Figure 4 shows the modeled supercontinuum for the $LP_{01,02}$ modes. Figures 4(a)-4(d) show the generated supercontinuum in the LP_{01} and the LP_{02} modes for three different pulse duration of 10, 40, and 60ps, respectively. For the 60ps pulse duration both modes obtained a noticeable amount of broadening with an octave occurring in both. The presence of anomalous dispersion close to the pump wavelength in the LP_{02} mode and not the LP_{01} mode generated different output spectra. The blue edge is, e.g., shorter in the LP_{02} mode due to the shorter first ZDW. The transfer of power between the modes and the underlying nonlinear processes become apparent by studying their individual power levels as the pulse propagated down the fibre as seen in Figs. 4(b)-4(e). Initially, the light was coupled into one of the LP_{01} polarisation. Due to the intermodal coupling to the co-polarised LP_{02} mode and the orthogonal polarisation of the LP_{01} mode, the pump pulse power was quickly reduced. The transfer of power into LP_{02} eventually stopped after about 20cm. As the intermodal coupling stopped, the transfer of power between the two polarisation in each mode through PMI followed, as was seen for the single LP_{01} mode shown in Fig. 3(b). For the shortest pulse durations considered, the 10ps pulse, there was negligible amount of power transferred into the LP_{02} as shown in Fig. 4(e). This was due to the Raman scattering not transferring light fast enough before the modes propagated away from each other due to walk-off cf. Fig. 1(c). The 40 and 60ps pulses allowed the light in the LP_{02} mode to built up and with increasingly larger amount for the longer pulse durations.

Comparing the spectra obtained with only the LP_{01} mode in Fig. 3 with the spectra obtained with both the LP_{01} and LP_{02} modes were present, the most noticeable difference was in that the pump and the first two Raman lines in Fig. 3(a) were not depleted as in Fig. 4(a). Furthermore, due to the strong Raman coupling between the modes less power was left in the LP_{01} mode when comparing power per mode in Figs. 3(b) and 4(b). Despite the strong intermodal Raman coupling the broadening for the two different cases were the same with the continuum extending out to around 5.5μm for the 60ps pulse duration. The PMI coupling between the two polarisations of the LP_{01} mode was still the most limiting factor when aiming at generating a broadband supercontinuum.

The way continua developed in both modes is seen from the contour plots in Figs. 4(g)-4(j). For the LP_{01} mode seen in Figs. 4(g)–4(h) the development was completely the same as for the single LP_{01} mode only shown in Fig. 3 where a few Raman lines built up in the pump pulse polarisation while at the same time PMI transferred power into the orthogonal polarisation. The continuum in the LP_{02} in Figs. 4(i)–4(j) mode began from the first Raman line at 3.11μm, which was generated after 10cm of propagation. The Raman stokes then underwent SPM broadening crossing into the narrow anomalous dispersion regime at 3.3-4μm (see. Fig. 1(d)) resulting in an octave spanning continuum. Similar dynamics occurred for the orthogonal polarisation of the LP_{02} mode where light was initially transferred through PMI from the co-polarised LP_{02} component, followed by subsequent broadening.

The supercontinuum generation taking into account the slightly weaker coupling between LP_{01} and LP_{11} mode was then considered. The LP_{11} mode is four times degenerate (2xHE_{21}, TE_{01}, and TM_{01}) and the coupling strength between the LP_{01} and these four LP_{11} components was identical. We therefore only consider the coupling to the two HE_{21} components of the LP_{11} mode. The dynamics between these four components is then described by Eq. (6), but as the HE_{21} mode were non-concentric the Raman coupling coefficients were equal meaning

#254943 Received 1 Dec 2015; revised 14 Jan 2016; accepted 16 Jan 2016; published 1 Feb 2016

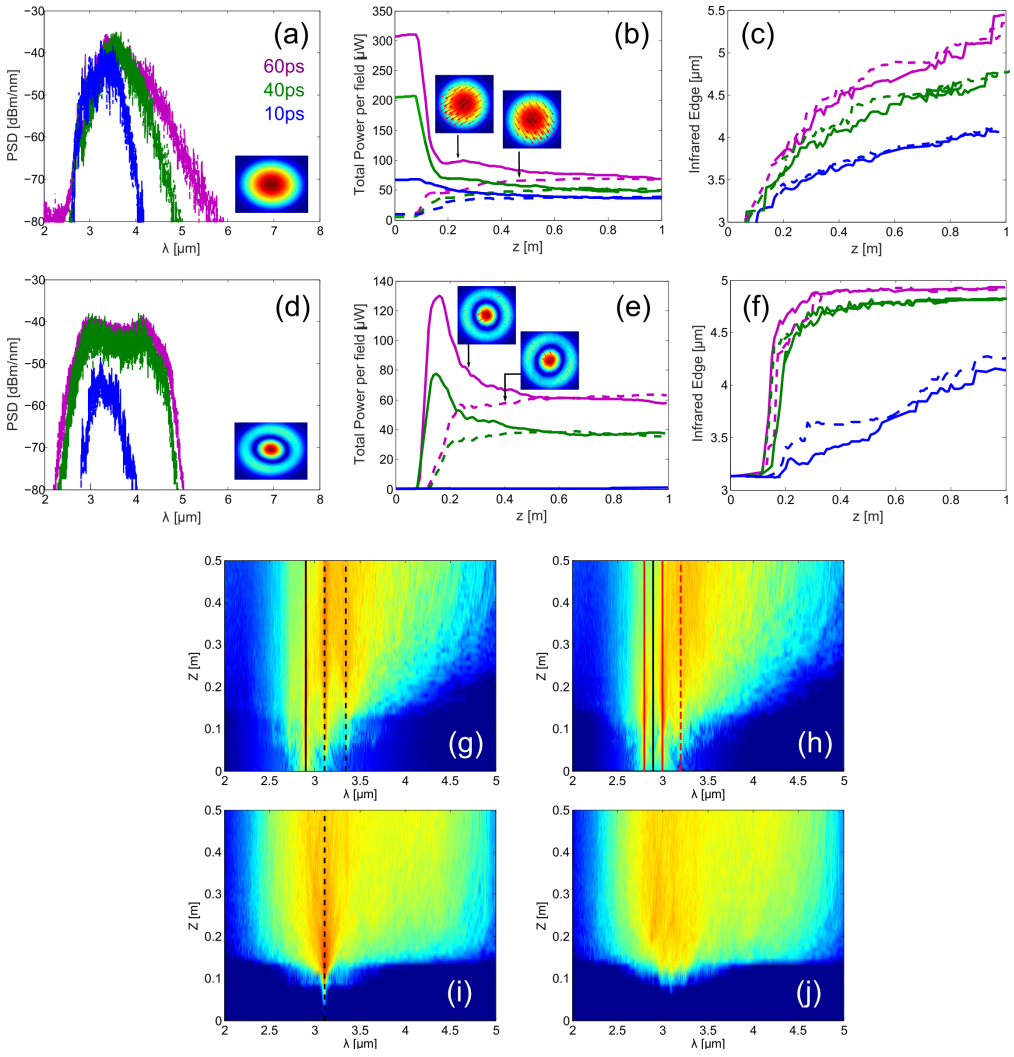

Fig. 4. (a) Supercontinuum generation in the LP_{01} mode at the end of one metre of fibre for different pump pulse durations. Inset: Spatial distribution of the mode. (b) Power distribution between the two polarisations of the LP_{01} mode. (c) Infrared edge at -30dB. The solid and dashed lines are for the pump polarisation and the orthogonal polarisation, respectively. (d)-(f) Same notation as before for the LP_{02} mode. (g) Contour plot of the LP_{01} continuum in the polarisation containing the pump pulse. The solid and dashed lines indicate the pump and the Raman lines, respectively. (h) Contour plot of the LP_{01}continuum in the orthogonal polarisation. The solid black and red lines indicate the pump and peak PMI gain bands, respectively, and the red dashed line is the first Raman line from the PMI stokes line. (i) Contour plot for the LP_{02} polarisation co-polarised with the LP_{01} polarisation containing the pump pulse. (j) Contour plot for the orthogonal LP_{02} polarisation.

that $Q_{1313}^{(1,2)} = Q_{1414}^{(1,2)} = Q_{2323}^{(1,2)} = Q_{2424}^{(1,2)} \neq 0$. The simulated results for a 60ps pump pulse are shown in Fig. 5. A 500nm broad spectrum is generated in the LP_{11} mode due to generation of two Raman lines. However, as expected the limited coupling between the modes, means that the

#254943 Received 1 Dec 2015; revised 14 Jan 2016; accepted 16 Jan 2016; published 1 Feb 2016

spectral broadening of the total field approximates that of the single LP_{01} mode supercontinuum generation.

We finally considered the even weaker coupling between the LP_{01} and LP_{21} modes. The LP_{21} mode was likewise four-fold degenerate containing the $2xEH_{11}$ and $2xHE_{31}$ components. The coupling strength to the four LP_{21} components is again the same and we limit the modeling to only take into account the $2xEH_{11}$ components for which $Q^{(1,2)}_{1313} = Q^{(1,2)}_{1414} = Q^{(1,2)}_{2323} = Q^{(1,2)}_{2424} \neq 0$. As expected the coupling to the LP_{21} mode can be neglected.

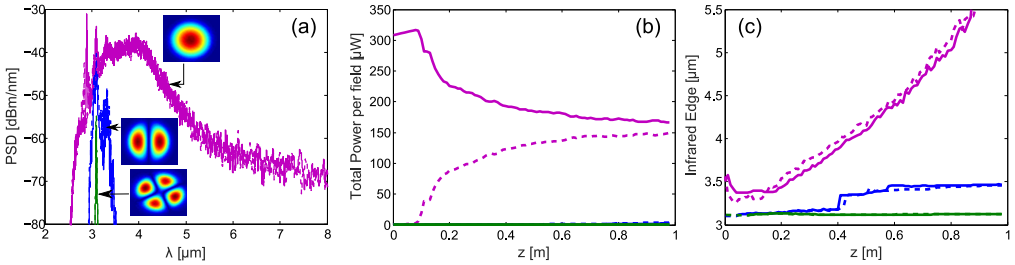

Fig. 5. Four component supercontinuum modeling of two separate two mode cases using a 60ps pump pulse as described in the text. Purple and blue show the LP_{01} and LP_{11} modes, respectively, when only these modes are considered. Purple and green show the LP_{01} and LP_{21} modes, respectively, when only these modes are considered. (a) Modal spectral profiles. (b) Power in the pump polarisation (solid) and orthogonal polarisation (dashed). (c) Infrared edge evaluated at -30dB.

If the $LP_{01,11,21,02}$ modes had been simulated together it would become apparent that only the LP_{02} mode would be excited while the others would get only negligible amount of power transferred to them. These results are in good agreement with previous studies of Raman scattering in multimode silica fibres where the Raman scattering occurred in the concentric LP_{0n} modes under optimum launch conditions where the laser light was predominately coupled into the LP_{01} mode [38–40].

Comparing the three different conditions studied here with the single LP_{01} polarisation, the single LP_{01} mode with both polarisation, and the LP_{01} mode in conjunction with HOMs the most detrimental effect in terms of generating the broadest supercontinuum was the coupling between the polarisations of the fundamental mode. The coupling between the modes through PMI depleted the pump before it could generated strong enough Raman lines that could broaden the spectrum. With the addition of the LP_{02} mode this became even worse as then the power in the LP_{01} mode got even more depleted. Since we were here using the co-polarised Raman response function, which is expected to stronger than the orthogonally Raman response function, to model all intermodal Raman scattering processes the power exchange between the $LP_{01,02}$ modes is expected to be here slightly exaggerated.

The power exchange between the modes can though be completely avoided by utilising pump pulses having shorter pulse durations as they do not drive intermodal Raman scattering as was seen in Fig. 4.

5. Conclusion

There is a current push towards developing high-average power mid-IR supercontinuum sources that cover the entire molecular fingerprint region with brightness orders of magnitude higher than the synchrotron. The hero experiments with high NA chalcogenide fibers (NA=1.0) and high peak power fs pumping in the anomalous dispersion region have shown that it is possible

#254943 Received 1 Dec 2015; revised 14 Jan 2016; accepted 16 Jan 2016; published 1 Feb 2016

to reach 13.3μm in a fiber [18]. However, the average power was too low for any practical applications. High average power mid-IR sources suitable for imaging and spectroscopy requires even higher NA fibers (NA=1.3-1.6) in addition to a pump laser with higher average power [16, 19, 20].

Mid-IR supercontinuum sources based on high-average power pump sources and high-NA chalcogenide fibers, typically means using long pulses and pumping in the normal dispersion regime of a highly multimode non-polarization maintaining (PM) fiber. This has been the topic of this detailed numerical study, in which we have focused on pumping at 2.9 um (such as the emerging laser wavelength of, e.g., Erbium doped ZBLAN fiber lasers) of a non-PM, high-NA chalcogenide step-index fiber with a zero-dispersion wavelength of 5μm and an NA of 1.0, as the one used in [18]. Q-switched lasers typically provide ns pulse lengths, so we have here pumped with a range of 10-60 ps pulse lengths in order to see the transition in the supercontinuum generation when going from ps towards the ns regime, over which the effect of temporal walk-off becomes less and less important.

We first determined which HOMs were important to take into account by looking at their specific dispersion profiles and the walk-off and coupling strength between them and the fundamental LP_{01} mode. This identified the $LP_{11,21,02}$ modes to be potentially important.

Standard single-mode scalar modeling using only one polarization of the LP_{01} mode was first shown to predict the generation of a supercontinuum reaching 20μm due to the strong nonlinearity of the chalcogenide fibre. We note that the 20μm is not realistic in that the IR loss edge of current chalcogenide fibers would limit it to around 13μm [18]. However, when considering both polarisations of the fundamental mode with the same pulse configurations (60ps pulse length, peak power 4.8kW), much less spectral broadening to only 5.5μm was observed. This was because PMI between the two polarisations of the LP_{01} mode was much stronger than the Raman scattering within the pump pulse polarisations. The investigation exemplified the importance of needing both polarisations when modeling SCG with the pump placed deep in the normal dispersion regime of the fibre.

Introduction of additional modes into the modeling depleted the pump pulse further of power as Raman scattering transferred power between the modes. The effect was strongest between the concentric modes due to their comparable fibre geometries, and this was in good agreement with previous experimental studies of intermodal Raman scattering in silica fibres [38–40]. A 2.2-5μm continuum was formed in the LP_{02} mode from the first LP_{02} Raman line at 3.1um generated by the pump at 2.9μm, which was close to the anomalous dispersion regime of the mode. The pump pulse duration was of crucial importance as it directly affected the efficiency of the Raman induced power transfer between the modes. For pulse durations $\leq$10ps no light was transferred between the modes, while for pulse durations $\geq$40ps power was transferred efficiently. This was due to the walk-off between the modes being long enough for power transfer to take place. The LP_{02} mode was therefore important to take into account when using ns pump pulses.

Acknowledgments

This research has been supported by the European Commission through the Framework Seven (FP7) project MINERVA (317803; www.minerva-project.eu). We thank Professor Karsten Rottwitt from the Dept. of Photonics Engineering at the Technical University of Denmark on fruitful discussion on Raman scattering in amorphous materials.

#254943 Received 1 Dec 2015; revised 14 Jan 2016; accepted 16 Jan 2016; published 1 Feb 2016